JOURNAL OF MATERIALS RESEARCH AND TECHNOLOGY 2022;19:1090–1101

Available online at www.sciencedirect.com

jmr&t Journal of Materials Research and Technology

journal homepage: www.elsevier.com/locate/jmrt

Original Article

Comparison of laser deposition methods for the synthesis of $Al_xCoCrFeNi$ multi-principal element alloy

Praveen Sreeramagiri [a], *Husam Alrehaili* [b], *Xin Wu* [b], *Guru Dinda* [c], *Ganesh Balasubramanian* [a,*]

[a] *Department of Mechanical Engineering & Mechanics, Lehigh University, Bethlehem, PA, 18015, USA*
[b] *Department of Mechanical Engineering, Wayne State University, Detroit, MI, 48202, USA*
[c] *Savannah River National Laboratory, Jackson, SC, 29831, USA*

ARTICLE INFO

Article history:
Received 17 March 2022
Accepted 16 May 2022
Available online 21 May 2022

Keywords:
Multi-principal element alloy
Additive manufacturing
Laser metal deposition
Powder bed fusion
Printability
Lattice strain

ABSTRACT

Additive manufacturing (AM) of multi-principal element alloys (MPEAs) has enabled high throughput synthesis for rapid alloy design and development for targeted structural properties. However, the complex solidification cycles endured by the material during processing often yield disparate outcomes when porting the processing conditions between different laser deposition techniques. With difference in the cooling rates being a primary difference between laser metal deposition (LMD) and powder bed fusion (PBF), understanding the effects of the processing on the microstructures and material properties is critical to assess the printability of such complex alloys. Here, we compare the fabricability, quality, and structural properties of $Al_xCoCrFeNi$ MPEA synthesized by LMD and PBF. Our results indicate that the equiatomic MPEA processed using PBF exhibits interfacial cracks due to warping and bending between successive deposit layers, while the LMD produces crack free near-dense deposits. XRD characterization corroborates a relatively high lattice strain of 1.8×10^{-3} in the PBF sample resulting from the high residual stresses arising from the relatively high cooling rates (~10^6 K/s) during the processing. While the PBF sample assumes smaller grains relative to the LMD processed alloy, no significant differences are noted in the crystallographic phases of the alloys produced by the two approaches. Also, the tool path employed to fabricate the alloy by LMD can facilitate gradation in the structural properties driven by the variation in thermal gradient during the synthesis. Further, we propose methods to map material space while porting processes within AM, enabling fabricability of alloys using PBF and DED.

* Corresponding author.
E-mail address: bganesh@lehigh.edu (G. Balasubramanian).

https://doi.org/10.1016/j.jmrt.2022.05.107

1. Introduction

Nickel-based superalloys have been addressing the need for high temperature materials in gas turbines to increase the operating temperatures (T) and achieve higher efficiency [1]. However, the demand for further pushing the envelope to operate gas turbines at T > 1600 °C, requires the discovery and development of novel alloys beyond the rather expensive Ni-superalloys. Recent interests in alloy exploration have encouraged a deviation from the conventional alloying strategies to explore the center of phase diagrams resulting in a new species of alloys *viz.*, multi-principal element alloys (MPEAs) [2]. In contrast to precipitation strengthened alloys, MPEAs feature single/dual phase solid-solutions (driven by the relatively 'higher' mixing entropy due to the comparable proportions of multiple constituent elements), which are stable at higher temperatures and aid in retaining superior mechanical, corrosive, and thermal properties even at an elevated T [2–18]. The prohibitively large compositional landscape available for MPEAs and the growing interest in accelerated alloy discovery using computational and machine learning techniques, has contributed to the research in high-throughput design of MPEAs with targeted properties [8,9,11,12,15,17,19–22]. Nevertheless, the validation of predicted phases/properties for these compositions at the lab scale has been typically limited to arc-melting [23,24], mechanical alloying, spark plasma sintering [25], and thin-film deposition [26]. The advancements in laser deposition based additive manufacturing (AM) techniques offer opportunities for high-throughput synthesis of MPEAs by increasing the scalability to marry alloy and component design for application-driven material properties [27–36]. However, the advantages associated with AM are occasionally superseded by manufacturing challenges that include porosity in the fabricated product and hot cracking of the component, arising from the residual stresses due to the high cooling rates employed (~10^3–10^6 K/s) [1,37,38]. While such rapid cooling rates contribute to reducing grain sizes in the alloys and consequently enhance the structural properties such as yield strength, such sharp temperature drops are detrimental for brittle materials. Controlling these cooling rates by optimizing the process parameters is essential for producing high quality deposits.

Another challenge lies in porting process parameters across various laser deposition methods, *viz.*, directed energy deposition (DED) and powder bed fusion (PBF), leading to disparities in the quality of the fabricated components and necessitating an entirely different process optimization approach. For instance, the AlCoCrFeNi MPEA that assumes a B2/BCC crystallographic phase upon solidification, is successfully realized with DED [29,32,40–48], while cracks are reported when using PBF techniques (specifically, selective laser melting/sintering) [49,50]. Typically, the machine dependent parameters such as the beam diameter of the heat source, the scan speed, and consequently the cooling rate induced during solidification, are predominantly responsible for these dissimilarities in the fabricated components; hence, it is important to understand the effects of these machine dependent processing parameters on the phases and properties of the alloy, especially when porting the parameters across different AM processes. While comparison between conventional methods like arc-melting and AM of alloys exist, only sparse knowledge is available on the structure and properties of the same alloy when processed with different AM techniques [49,51]. To address this gap, we conduct a systematic investigation on the processability, formation of cracks, and presence of porosity for $Al_xCoCrFeNi$ MPEA synthesized using two AM processes *viz.*, the laser metal

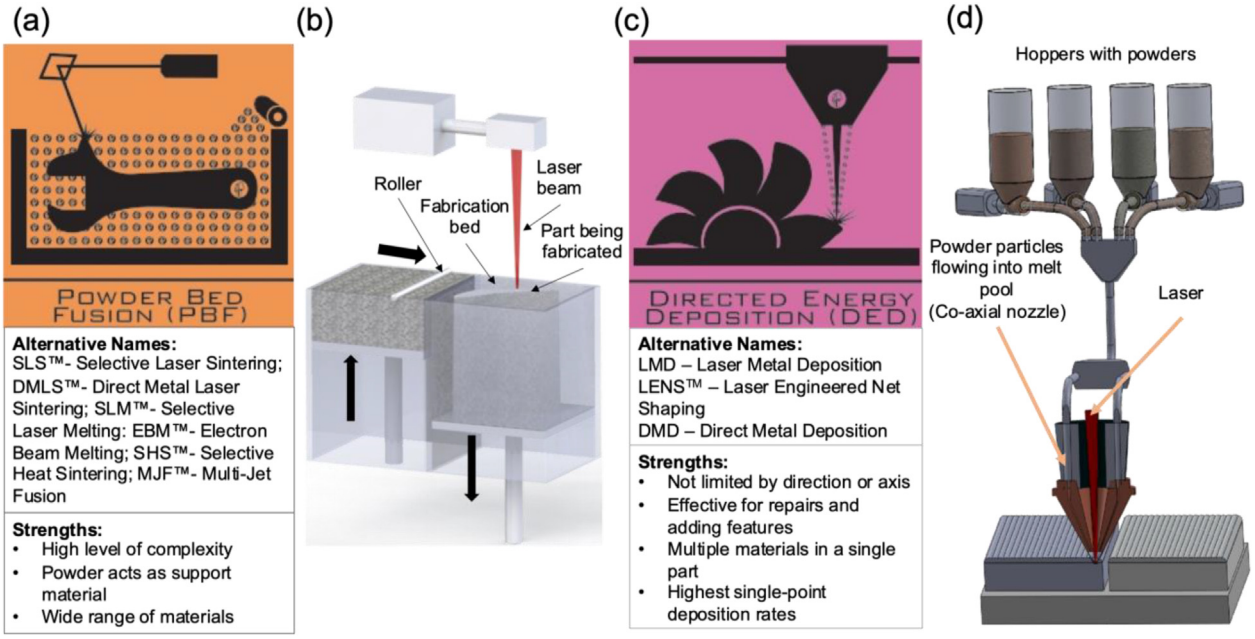

Fig. 1 – An infographic of the powder bed fusion (PBF) and the directed energy deposition-based laser metal deposition (LMD) processes as described by ASTM [37,39].

Table 1 – Processing parameters employed for the synthesis of the equiatomic AlCoCrFeNi MPEA.

	LMD	PBF
Powder Size	45–150 μm	5–50 μm
Laser Power	600–800 W	50–300 W
Hatch Distance	1 mm	0.05–0.09 mm
Velocity	500–800 mm/min	1–2 m/s
Powder flow rate	24–28 gm/min	N/A
Layer thickness	0.6 mm	0.03 mm
Substrate	In 718, SS 316	Ni, SS316
Energy Density (J/mm^3)	50–200	

deposition (LMD) and the selective laser melting (SLM, interchangeably denoted as PBF). As described below, LMD produces higher quality deposits relative to PBF, which produces samples with cracks resulting from warping and bending of the deposited layers during fabrication.

2. Experimental methods

We utilize the custom-built laser metal deposition equipment at the Wayne State University and the commercial Renishaw AM400 at the Lehigh University to synthesize the $Al_xCoCrFeNi$ MPEA using LMD and SLM, respectively. Fig. 1 presents an infographic for the two manufacturing approaches. We use gas atomized, spherical equiatomic AlCoCrFeNi and CoCrFeNi alloy powder (Elemental Metals) with rolled In718, Ni and SS 316 as substrate materials for both the processes. The individual material and process parameter details for the LMD and PBF are listed in Table 1. The energy densities obtained from a previous predictive framework are employed [52]. Further, we conduct design of experiments (DoE) with more than 100 samples using optimal Latin hypercube sampling (OLHS) [53] for PBF, and the traditional factorial method (1/3rd factorial) using 12 samples for LMD to obtain optimum process parameters. Each fabricated sample embodies a unique set of processing parameters in the design matrix within the range as specified in Table 1. Finally, the samples that exhibit high density are selected for detailed characterization. We choose the optimization strategies based on the resolution of the process and the number of samples synthesized. In addition, the LMD samples are processed in cylindrical shapes with the laser moving from inside to out of the deposit as shown in Fig. 2(a). In contrast, the PBF samples are deposited in cuboidal shapes with a conventional meander tool path that scans in hatch pattern (Fig. 2(b)), with a 67° offset in every layer.

Upon syntheses, the samples are prepared for microstructural characterization by cutting, mounting, and polishing with grit papers ranging from 180 to 1200, followed by 0.05 μm colloidal silica. We conduct X-ray diffraction using the Bruker D8 X-ray Diffractometer with a Cu-Kα radiation (λ = 0.154 nm, 50 kV, 1000 μA) and crystallography analysis using the GSAS-II open-source software [54]. Microstructural characterization is performed using Hitachi S-4300SE and JEOL 7100 F with an accelerating voltage of 20 KeV and a beam

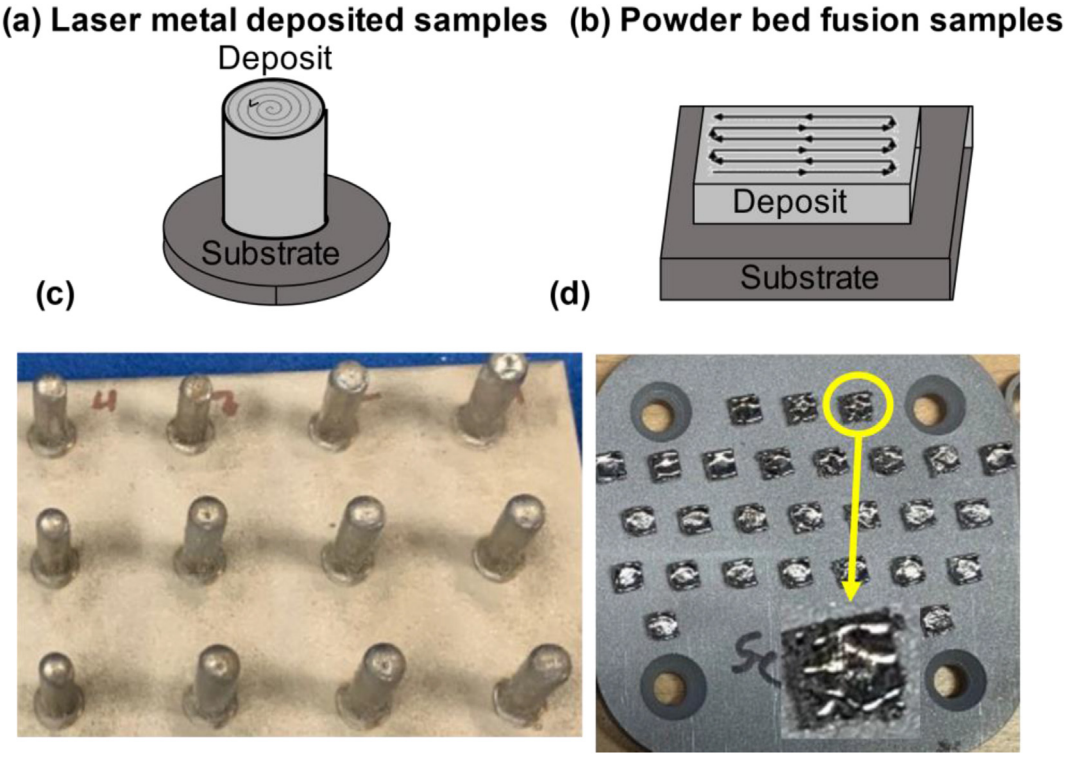

Fig. 2 – Samples processed with (a) Cylinder components with laser moving from inside to out of the deposit to fabricate samples with the LMD process; (b) Meander tool path with cross-hatch pattern to deposit cuboidal samples using the PBF technique; (c) Laser metal deposited samples are free from major defects such as flaking and cracks; (d) Powder bed fusion fabricated samples reveal significant flaking and cracking due to high residual stresses during processing. The inset illustrates a magnified view of a representative sample with pointed edges signifying the warp during fabrication.

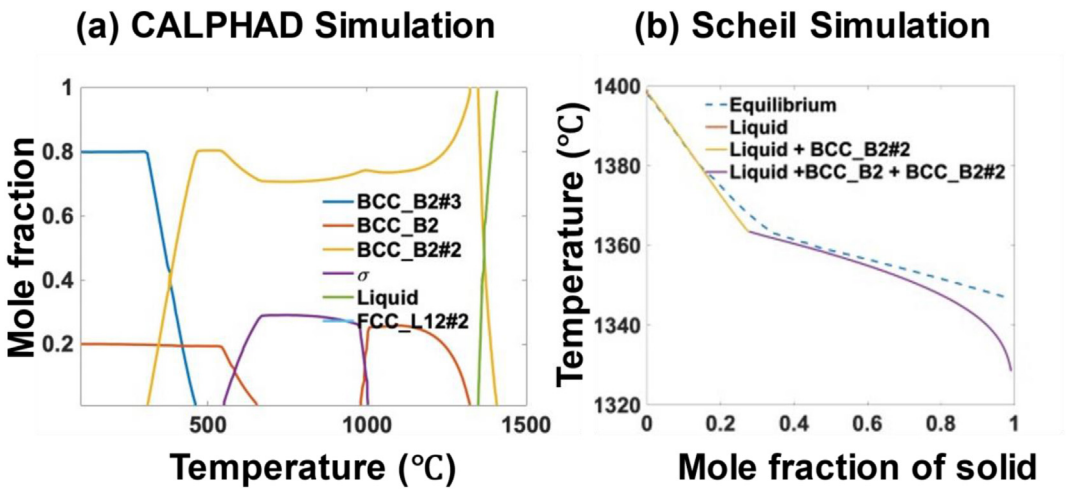

Fig. 3 – (a) CALPHAD simulation suggests a low precipitate volume fraction, while the σ phase is presumed to precipitate at long term exposures to high temperatures, (b) Scheil simulation reveals a low temperature difference between solidus and liquidus temperatures, suggesting less susceptibility to solidification cracking.

current of 5 nA. The microstructural features reported are post polishing and no etching is performed to reveal the precipitates. Further, we employ energy dispersive X-ray spectroscopy using the EDAX Octane Elect Plus and the Oxford Ultim Max detector to conduct elemental analysis and mapping. Microhardness measurements are performed using LECO LM248 hardness testing equipment with a 100-gf load and a spacing of >1 mm between each indent on the LMD samples and ~100 μm for the PBF samples. The shorter distance used for the PBF samples is due to the associated smaller sample volume.

3. Results and discussion

3.1. *Assessing the printability*

Fig. 2 (c & d)reveals the samples processed using both the methods. It is interesting to note that the samples processed using PBF possess significant number of cracks notwithstanding the wide range of process parameters employed, while the samples synthesized by LMD produce high quality deposits with no noticeable defects. In addition, we interrupt the PBF process prior to completion of the deposition due to the frequent tearing of the powder coater as the samples are consistently disrupted during processing. To understand this discrepancy between the two processes, we examine the thermodynamic stability of the materials using CALPHAD and Scheil simulations. The calculated phase diagram using the Thermo-Calc HEA database [55] and the associated Scheil cooling diagrams are presented in Fig. 3. The simulation results suggest a low precipitate volume fraction with ~20% precipitates in the alloy, indicating good printability. While the predictions corroborate the formation of σ phase, these unfavorable phases usually precipitate at long term exposure to high temperatures and are not anticipated during AM fabrication that employs very high cooling rates. Likewise, the Scheil simulation reveals a relatively small difference of

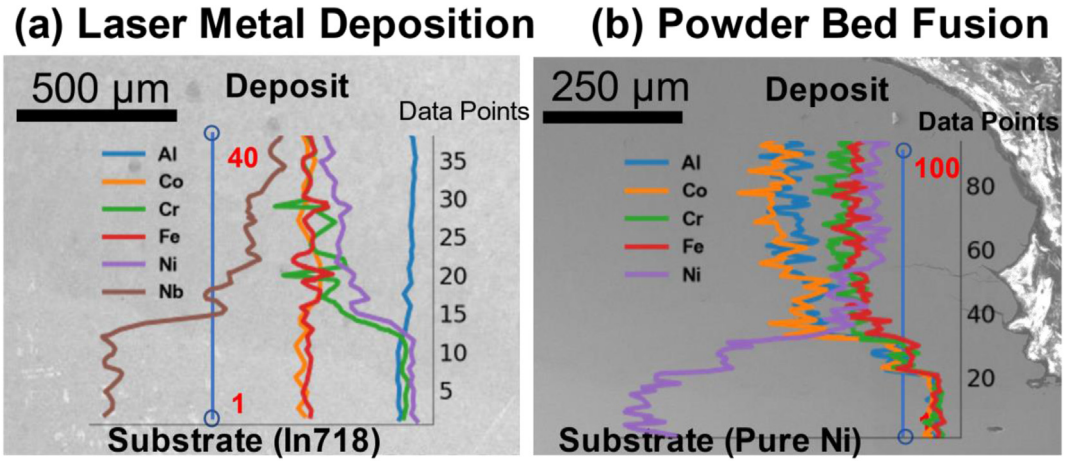

Fig. 4 – SEM images of samples processed by (a) LMD and (b) PBF reveals a homogenous dilution at the interface from substrate to deposit with clean crack-free interface. EDS line scan from substrate to deposit indicates an uncontaminated dilution that is free from intermetallics at the interface.

~80 °C between solidus and liquidus temperatures, recommending printability by promoting uniform solidification of molten metal initiating at the dendrite core and leaving sufficient liquid fraction at the end of solidification in the interdendritic zones. This phenomenon reduces the chances for mushy zones and consequently the liquation crack susceptibility due to tensile forces in liquid [1,38,56].

3.2. *Analyzing substrate-deposit compatibility*

The substrate material has a significant effect on the cracks that can propagate in the deposit [41]. The literature on AM of $Al_xCoCrFeNi$ suggests the use of SS316 as a substrate material since its coefficient of thermal expansion (CTE) is similar to that of the deposited alloy [41,50,57,58]. Besides the CTE, understanding chemical compatibility is important to avoid the formation of brittle intermetallics that lead to cracking at the interface during the processing. Considering both the CTE and chemical compatibility, we use alloys SS316, In718 and Ni as substrate materials, because they have several common candidate elements and can prevent the occurrence of brittle intermetallics. Further, the SEM characterization reveals no secondary brittle phases at the substrate-deposit interface for both the samples. Additionally, the EDS line scan (Fig. 4)

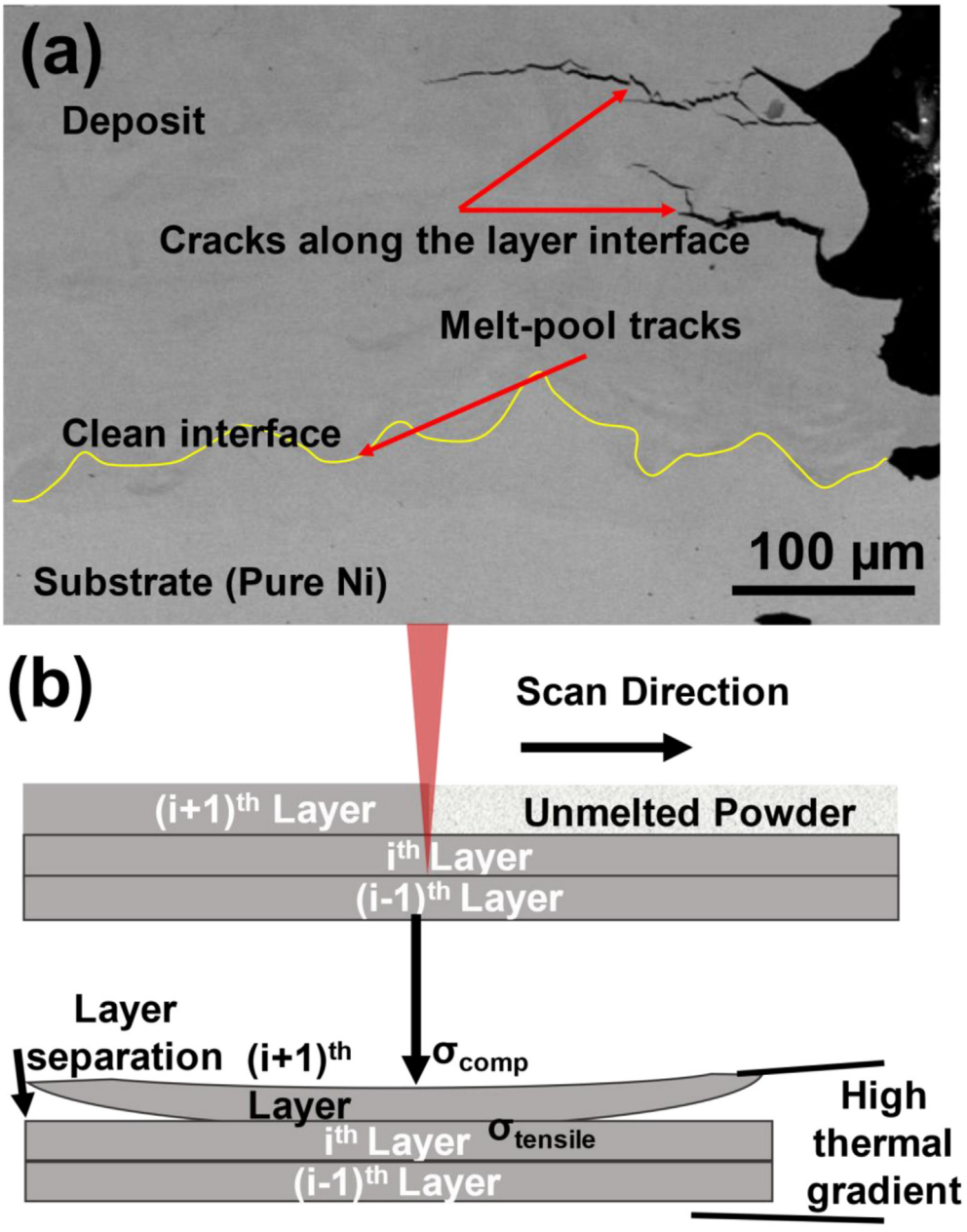

Fig. 5 – (a) Back scatter electron characterization of the PBF sample reveals the melt-pool boundaries, and the laser scan tracks together with the layer interfaces. Cracks are noted at the layer boundaries due to the process induced thermal stresses. (b) A schematic illustrating the crack formation mechanism in the $(i+1)^{th}$ layer due to the induced high compressive and tensile forces as a consequence of the steep thermal gradient.

reveals a smooth transition of candidate elements (Ni, Nb in718 for LMD, and Ni for PBF) from substrate to deposit in the dilution zone. The compositional analysis in line scan validates that the dilution is crack free with no potential intermetallics manifested. Therefore, we assert that the substrates used are compatible with the deposit material for both LMD and PBF.

3.3. *Crack formation mechanism in the PBF samples*

With the substrate-deposit compatibility and material printability ruled out as the causes for crack formation, we next scrutinize the PBF sample to understand the crack formation mechanism. The absence of crack density quantification is a limitation of the current study, but the maximum possible build height (h) without warping being <1 mm, we scrutinize the samples that do not warp with h < 700 μm to understand the origin of the cracks. Fig. 5 reproduces the back-scatter electron characterization of the PBF sample with various grain orientations, melt-pool tracks, layer and bead boundaries. The cracks in the sample are at the layer boundaries, suggesting high residual stresses [59]. Upon solidification of the i^{th} layer, a thin layer of powder is coated on the existing layer for the $(i+1)^{th}$ layer. When a laser beam passes through this layer of powder and the solidified layers underneath, the temperature variation from the top layer to the substrate is considerable, creating a steep thermal gradient from the high cooling rates (~10^6 K/s). The latter induce enormous residual stresses in the alloy post solidification [18]. Simultaneously, the expansion (due to melting) and contraction (due to solidification) of the top layer relative to the layers that are underneath, creates a compressive stress above the top layer, while exerting a tensile stress below the same layer. These combined tensile and compressive forces (due to the high residual stresses exerted on the ordered B2 matrix) cause the material to bend and detach from the previous layers, triggering a failure in the deposit by warping (illustrated in Fig. 5(b)). In contrast, the samples fabricated using LMD circumvent these effects due to relatively low cooling rates (~10^3 K/s), and produce crack-free high-quality deposits. In addition, quantifying the crack density is limited due to the insufficient build volumes (height <1 mm) and the occurrence of severe warping beyond 700 μm build height.

3.4. *Quantifying the lattice strain*

To understand the effects of high cooling rates on the residual stresses, we perform XRD analyses on the LMD and PBF samples to quantify the lattice strain exhibited during solidification. Lattice strains in crystalline solids can be quantified using peak broadening analyses, which usually occur when the crystallite size/atom positions drift from the ideal configuration [15]. Fig. 6 presents the XRD analyses of the samples. The peak locations for both samples insinuate the formation of B2/BCC phase with trace amounts of FCC as displayed in Fig. 6 (a).

We perform Williamson Hall analysis, as mentioned elsewhere [60], to quantify the crystallite strain. Fig. 6 (b) displays the full width half maximum (FWHM) values for both samples as a function of 2θ. A qualitative analysis of the FWHM suggests a high peak broadening on the PBF sample relative to that for the LMD sample. Quantitatively, we find a strain of 1.8×10^{-3} in the PBF sample, which is higher than the strain exhibited by LMD processed sample (1.4×10^{-3}), thus validating our hypotheses that the failure in the PBF samples is due to the high resultant strain arising from the relatively higher cooling rates. We conclude that the material producing high quality deposits from one AM process may not yield the same outcomes with a different process even if they have the same heat source. Nevertheless, the quality/fabricability depends on the material properties and the selected process parameters.

3.5. *Microstructural characterization*

Fig. 7 displays the microstructural evolution post LMD and PBF of AlCoCrFeNi with the respective chemical compositions. Table 2 validates that the final composition of the deposited

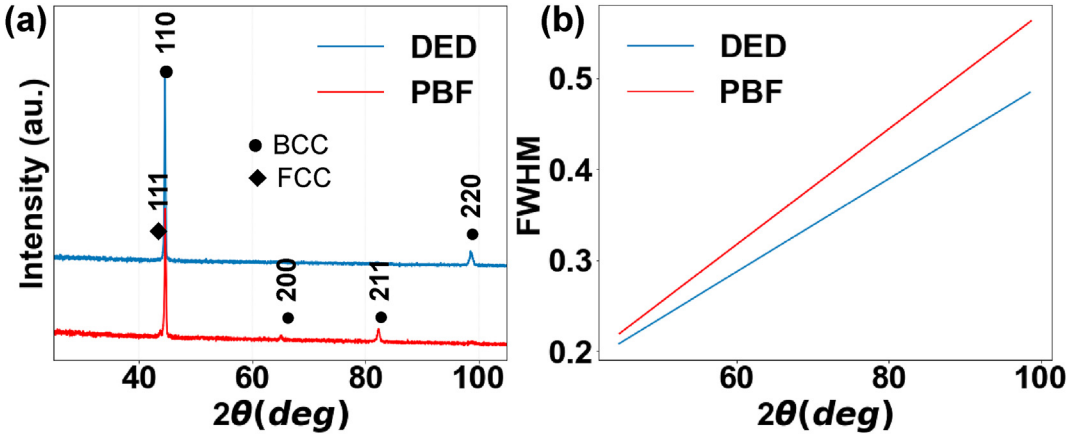

Fig. 6 – (a) X-Ray diffraction on the PBF and LMD samples endorse the dominant B2/BCC phase with infinitesimal fraction of FCC realized upon solidification. (b) Comparison of the full width half maximum (FWHM) values suggest a higher peak broadening of PBF processed samples relative to those processed using LMD, corroborating the formation of smaller grains and higher lattice strains for the PBF processed samples.

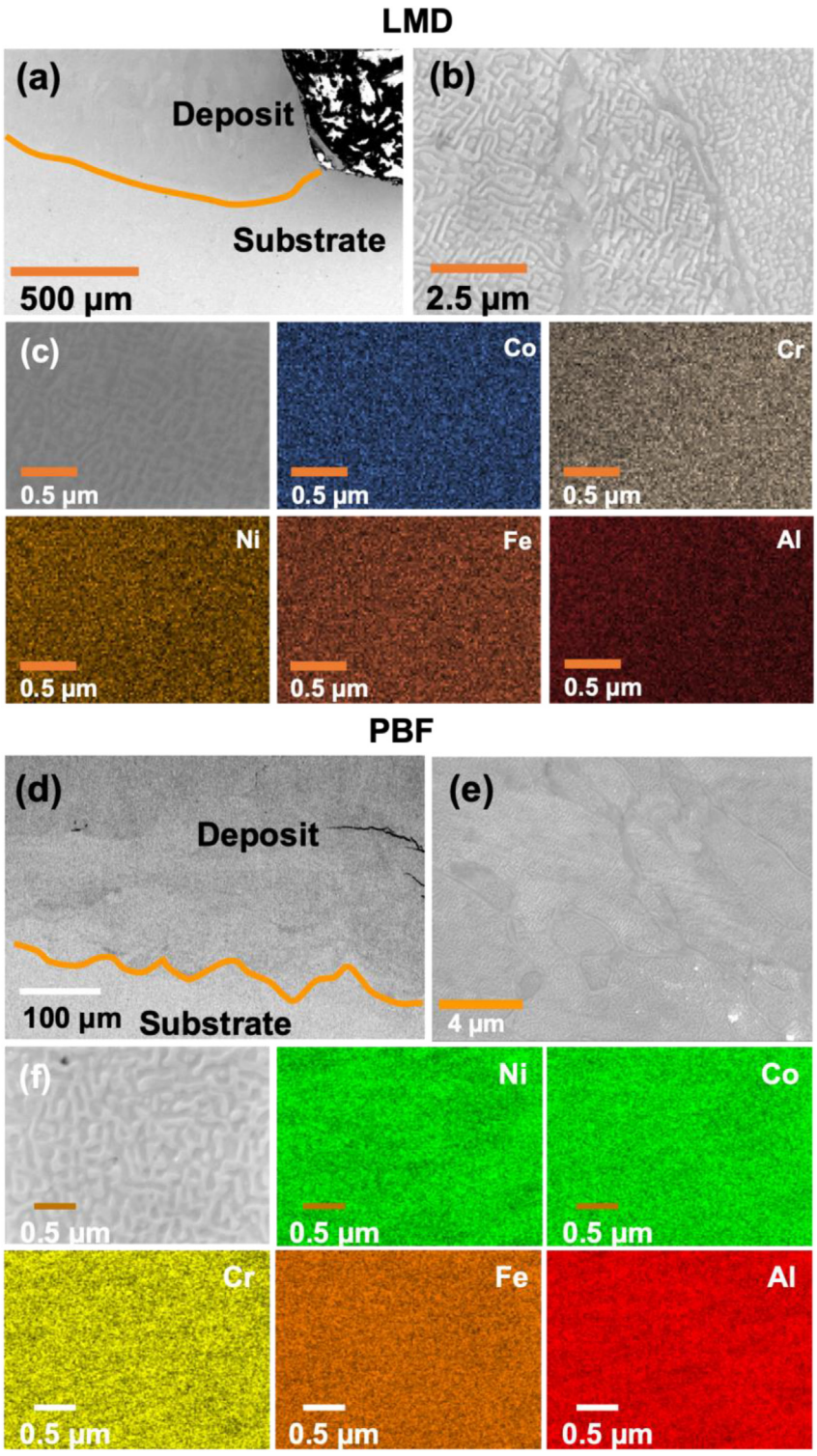

Fig. 7 – SEM characterization of AlCoCrFeNi deposited using LMD and PBF processes (a,d) Macroscopic image showing the substrate-deposit interface for LMD and PBF, respectively (the line showing the interface has been raised relative to the interface to reveal the feature) (b,e) Continuous and island like BCC precipitates are recorded in the B2 matrix along with the grain boundaries populated with FCC (c,f) EDS mapping on the samples reveals a homogenous distribution of the candidate elements.

Table 2 – Elemental compositions of the alloy deposited using LMD (associated with Fig. 7 (b)).

Element	Al	Cr	Fe	Co	Ni
Weight %	11.29	24.11	23.06	21.45	20.1
Atomic %	20.9	23.17	20.63	18.18	17.11

alloy agrees with the equiatomic composition. Fig. 7(a,d) reproduce the substrate-deposit interface of LMD and PBF processed samples, respectively, along with the melt-pool boundary. As the laser advances from the initial position, the melt-pool rapidly cools down, resulting in a steep temperature gradient. To attain an energetic equilibrium with the temperature variations, heterogenous nucleation is initiated near the substrate solid–liquid interfacial boundary. Following nucleation, crystal growth trails the direction opposite to that of the heat flow, *i.e.*, the build direction. This mechanism promotes the growth of epitaxially guided columnar grains near the substrate-deposit interface as shown in Fig. 7(a) [1].

On further interrogation, the grains from both the LMD and the PBF samples reveal the formation of precipitates. Literature on $Al_xCoCrFeNi$ MPEA suggests a BCC matrix with B2 precipitates as a function of x; the phase is transformed to a B2 matrix with BCC precipitates for $x > 0.8$ together with traces of FCC in the grain boundaries [61]. Congruent to these observations, we identify a B2 matrix with several coherent continuous and island-like BCC precipitates realized upon solidification within the grains alongside FCC grain boundaries. However, the high cooling rates in PBF lead to relatively smaller grains (2–10 μm) as evinced in Fig. 7(e), while the grains of the LMD sample are larger, measuring up to few tens of microns (4–40 μm). Furthermore, the grain boundaries in all these samples are populated with FCC precipitates as shown in Fig. 7(b,e). Also, Fig. 7 (c,f) illustrate the EDS mapping on both the samples, revealing a homogenous compositional distribution in the deposit. Our observations are in agreement with the literature on the DED of AlCoCrFeNi MPEA [49].

3.6. *Effect of tool path on the local microstructures*

We investigate the role of the tool path on the evolution of the local microstructures and hence the mechanical properties. The tool paths employed for deposition are as discussed in the experimental section above. Accordingly, we consider hardness in the XY direction for the LMD processed sample, and along the Z direction for PBF sample to understand the effect of the tool path (as illustrated in Fig. 2 (a & b)) on the local hardness. The choice of the test planes and the respective scales for the reported results are based on the volume of the sample available in the corresponding planes. Fig. 8 presents the variation of hardness in the LMD and PBF samples. To reproduce a trend, the results are sampled near the edges and the center of deposit with ~10 measurements in each location to present the hardness at three locations (two edges and one center) for the LMD processed sample as illustrated in Fig. 8(a). On the other hand, the hardness for PBF sample is measured

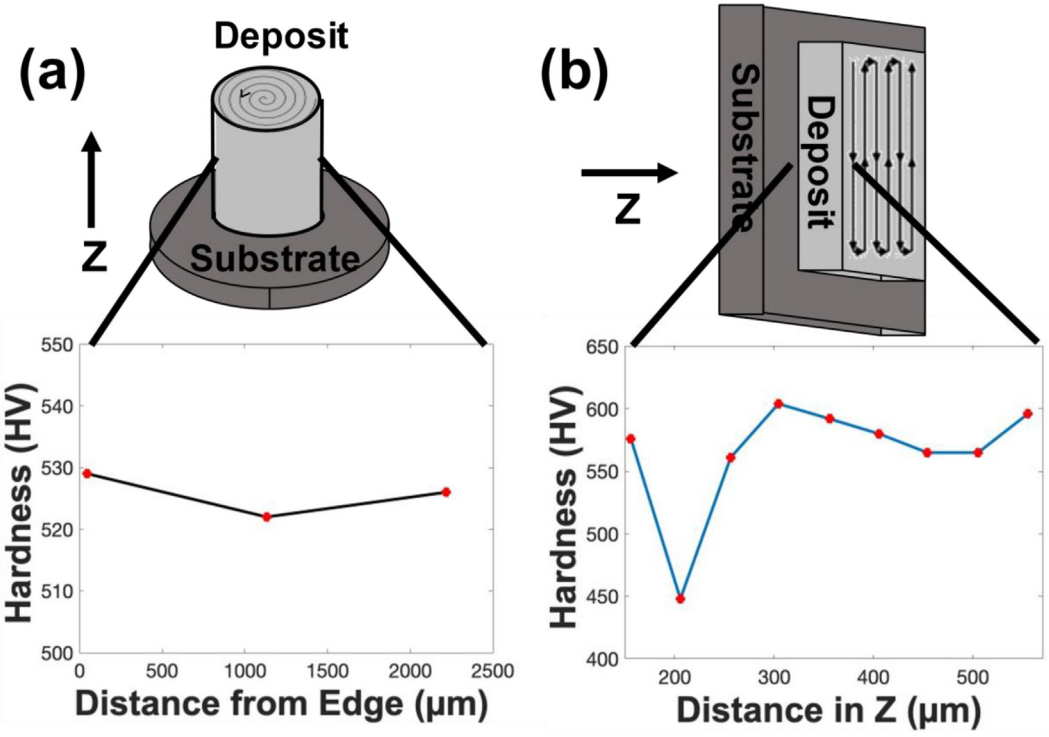

Fig. 8 – Variation of hardness as a function of distance attributed to the heat flow. (a) The hardness variation from left to right edge in the LMD sample that suggests a higher hardness at the edges and a relatively softer center, is attributed to the change in thermal gradients due to the tool path employed. (b) The change in hardness from interface to the top of the deposit in the build direction reveals a random hardness change as the deposition progresses along the z direction.

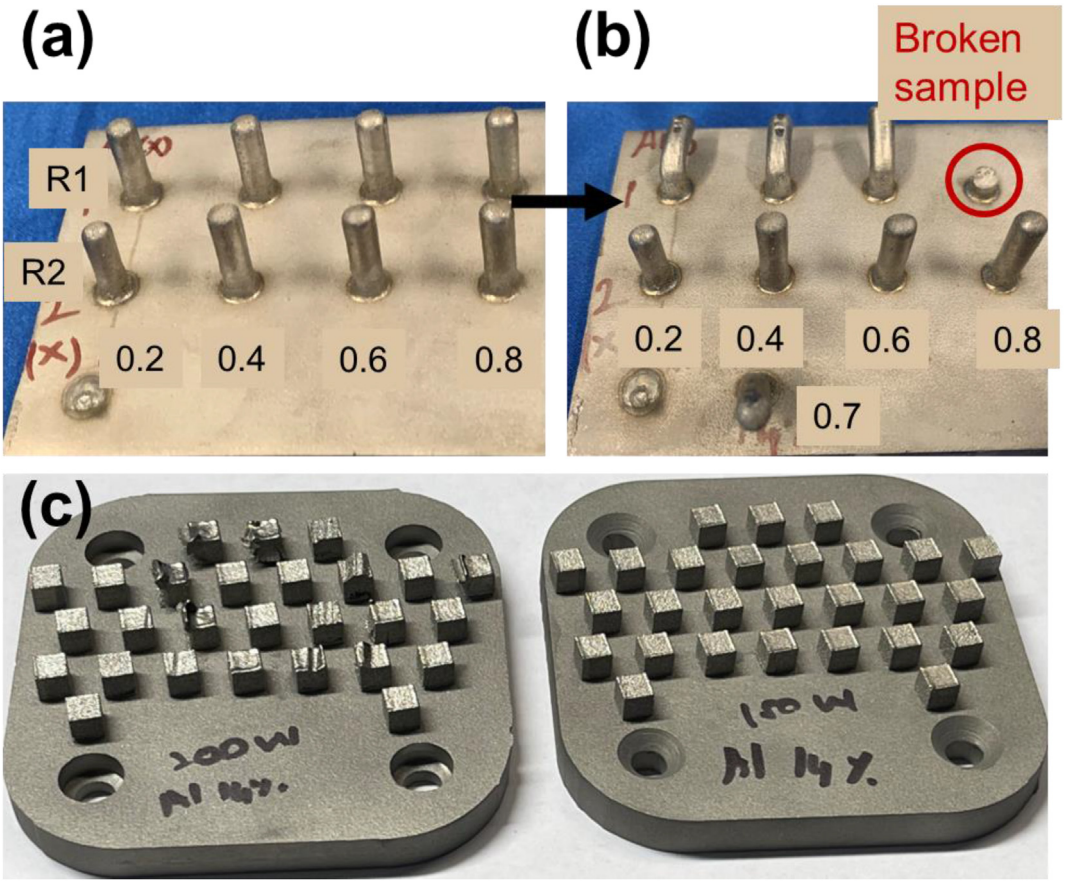

Fig. 9 – (a) Combinatorial synthesis of $Al_xCoCrFeNi$ MPEA with $x = 0.2, 0.4, 0.6, 0.8$. Here R1 and R2 correspond to two samples processed using the same processing parameters. (b) Bending the synthesized coupons to qualitatively estimate the ductility of the alloys and iterating through the compositions to fabricate an alloy with $x = 0.7$. Results reveal that $Al_xCoCrFeNi$ MPEA with $x = 0.7$ attains a reasonable ductility and can be fabricated with both the processes. (c) $Al_{0.7}CoCrFeNi$ MPEA synthesized with PBF shows no visible cracks or warps over two iterations indicating fabricability.

along the Z-axis due to the sample size limitations from build height and warping in the XY-plane.

The results suggest a relatively high hardness along the edges of LMD processed sample, with a lower hardness in the center owing to the thermal transport. As the laser is turned on in the center and progresses towards the edge, a high heat flux persists at the edge due to convectional and radiative cooling from the surroundings in addition to conduction. The center, which is the initial location of the laser, experiences a reduced thermal gradient due to prolonged exposure to high temperatures as a function of laser holding time. However, the lack of a uniform pattern/trend for the hardness evolution in the PBF sample as a function of build height is attributed to the heating and cooling of material during deposition. Also, the lattice strains in the PBF samples contribute to a higher overall hardness relative to that for the LMD processed sample.

4. Conclusion

We present results from additive manufacturing of Al_x-CoCrFeNi MPEA using two processes *viz.*, laser metal deposition (LMD) and powder bed fusion (PBF). Our results reveal that the samples processed through LMD produce high quality deposits, while those fabricated through PBF exhibit cracks that are characterized at the interfaces between subsequent layers deposited. These interlayer cracks lead to failure during deposition by warping and bending. XRD analyses on the samples corroborate the formation of B2/BCC crystallographic phases with traces of FCC realized from the build. Strain quantification using Williamson-Hall analysis reveals a high lattice strain of 1.8×10^{-3} in the PBF samples with a relatively lower strain reported for the LMD sample (1.4×10^{-3}). The estimated lattice strains suggest that cracks in PBF samples occur due to the high residual stresses as a consequence of the high cooling rates during deposition (~10^6 K/s), unlike for the LMD process with relatively low cooling rates (10^3 K/s). Microstructural characterization on both sets of samples reveals a B2 matrix with continuous and island like BCC precipitates within the grain core and FCC precipitates in the grain boundaries. However, the higher cooling rate exerted on the alloy during PBF results in relatively smaller grains compared to that of the LMD processed samples. In addition, the tool path employed to deposit the material influences the local properties due to changes in the local thermal gradients. Our results suggest that a material that can yield high quality

deposits under a specific AM process may not yield the similar characteristics with a different AM technique, even when employing a similar energy source for producing the alloy melt.

5. Outlook

Based on the results from the experimental builds and characterizations, we believe that DED approaches are more conducive for rapid alloy discovery, while scalable component fabrication using PBF can offer the highest achievable resolution with the current state-of-the-art platforms. Nonetheless, the quality of the builds produced from both the processes has significant room for improvement. DED can produce high quality components on geometries with minimum to no overhangs; in contrast, complex geometries that require supports (e.g., porous structures), specifically for applications involving medical implants, can be fabricated with relative ease using the PBF process. In the latter, the powder bed acts as support facilitating fabrication to a certain extent of overhang. Thus, in the context of alloy development for AM, an interrogation of the component fabrication using both methods is essential, accounting for the processing limitations of alloys for the respective techniques.

In the same vein, we propose a method to foster rapid alloy discovery using DED with emphasis on the fabricability via both the processes. We initiate with a combinatorial approach to deposit four different compositions of Al_x-CoCrFeNi MPEA with $x = 0.2, 0.4, 0.6, 0.8$, as displayed in Fig. 9(a), with a laser power of 700 W and a 700 mm/min scan speed, selected using process parameter optimization. The findings from the DoE advocate that Al_xCoCrFeNi MPEA does not crack despite the wide processing envelope employed; these findings suggest that process parameters relevant for alloy discovery do not alter the results significantly [61]. In addition, R1 and R2 in Fig. 9(a) refer to the samples fabricated twice with the same processing parameters and composition to aid in the illustration. Upon fabrication, we bend these samples using conventional pliers to qualitatively investigate the ductility by visually inspecting the extent of bending in these alloys. While obtaining quantitative estimates of ductility is beyond the scope of this work, we utilize this qualitative analysis to map the composition space from one process to the other. As can be noted in Fig. 9(b), the sample with $x = 0.8$ marginally bends and breaks revealing minimal ductility. Iterating further, we fabricate a composition with $x = 0.7$, which demonstrates bending without breaking. Subsequently, fabricating Al_x-CoCrFeNi MPEA with $x = 0.7$ using PBF reveals no visible cracks within two iterations, suggesting the alloy is fabricable with PBF. Thus, we utilize DED to map the material space when porting process parameters across AM platforms to identify compositions compatible with both DED and PBF. We acknowledge that continued efforts are required to establish quantitative metrics for porting the material selection and optimal process parameters for successful component fabrication across different AM platforms.

Declaration of Competing Interest

The authors declare that they have no known competing financial interests or personal relationships that could have appeared to influence the work reported in this paper.

Acknowledgements

The research was supported by the National Science Foundation (NSF) through the award # CMMI-1944040. Any opinions, findings, conclusions, or recommendations expressed in this material are those of the authors' and do not necessarily reflect the views of the NSF.

REFERENCES

[1] Sreeramagiri P, Bhagavatam A, Alrehaili H, Dinda G. Direct laser metal deposition of René 108 single crystal superalloy. J Alloys Compd 2020;838:155634. https://doi.org/10.1016/j.jallcom.2020.155634.

[2] Cantor B, Chang ITH, Knight P, Vincent AJB. Microstructural development in equiatomic multicomponent alloys. Mater Sci Eng, A 2004:213–8. https://doi.org/10.1016/j.msea.2003.10.257. 375–377.

[3] Yeh JW, Chen SK, Lin SJ, Gan JY, Chin TS, Shun TT, et al. Nanostructured high-entropy alloys with multiple principal elements: novel alloy design concepts and outcomes. Adv Eng Mater 2004;6:299–303. https://doi.org/10.1002/adem.200300567.

[4] Cantor B. Multicomponent and high entropy alloys. Entropy 2014;16:4749–68. https://doi.org/10.3390/e16094749.

[5] Thurston KVS, Gludovatz B, Yu Q, Laplanche G, George EP, Ritchie RO. Temperature and load-ratio dependent fatigue-crack growth in the CrMnFeCoNi high-entropy alloy. J Alloys Compd 2019;794:525–33. https://doi.org/10.1016/j.jallcom.2019.04.234.

[6] George EP, Raabe D, Ritchie RO. High-entropy alloys. Nat Rev Mater 2019;4:515–34. https://doi.org/10.1038/s41578-019-0121-4.

[7] Li W, Liaw PK, Gao Y. Fracture resistance of high entropy alloys: a review. Intermetallics 2018;99:69–83. https://doi.org/10.1016/j.intermet.2018.05.013.

[8] Singh P, Sharma A, Smirnov AV, Diallo MS, Ray PK, Balasubramanian G, et al. Design of high-strength refractory complex solid-solution alloys. Npj Computational Materials 2018;4:16. https://doi.org/10.1038/s41524-018-0072-0.

[9] Sharma A, Deshmukh SA, Liaw PK, Balasubramanian G. Crystallization kinetics in AlxCrCoFeNi ($0 \leq x \leq 40$) high-entropy alloys. Scripta Mater 2017;141:54–7. https://doi.org/10.1016/j.scriptamat.2017.07.024.

[10] Sharma A, Singh R, Liaw PK, Balasubramanian G. Cuckoo searching optimal composition of multicomponent alloys by molecular simulations. Scripta Mater 2017;130:292–6. https://doi.org/10.1016/j.scriptamat.2016.12.022.

[11] Khakurel H, Taufique MFN, Roy A, Balasubramanian G, Ouyang G, Cui J, et al. Machine learning assisted prediction of the Young's modulus of compositionally complex alloys. Sci Rep 2021;11(1):1–10. https://doi.org/10.1038/S41598-021-96507-0. 2021;11.

[12] Singh R, Sharma A, Singh P, Balasubramanian G, Johnson DD. Accelerating computational modeling and

design of high-entropy alloys. Nature Computational Science 2021;1:54–61. https://doi.org/10.1038/s43588-020-00006-7.
[13] Osei-Agyemang E, Balasubramanian G. Effect of oxidation on the thermal expansion of a refractory multicomponent alloy. Phil Mag Lett 2021;101:173–82. https://doi.org/10.1080/09500839.2021.1881641.
[14] Sharma A, Singh P, Johnson DD, Liaw PK, Balasubramanian G. Atomistic clustering-ordering and high-strain deformation of an Al0.1CrCoFeNi high-entropy alloy. Sci Rep 2016;6:31028. https://doi.org/10.1038/srep31028.
[15] Roy A, Sreeramagiri P, Babuska T, Krick B, Ray PK, Balasubramanian G. Lattice distortion as an estimator of solid solution strengthening in high-entropy alloys. Mater Char 2021;172:110877. https://doi.org/10.1016/j.matchar.2021.110877.
[16] Sharma A, Levitas VI, Singh P, Basak A, Balasubramanian G, Johnson DD. Twinning-induced pseudoelastic behavior in (MoW)$_{85}$(TaTi)$_{7.5}$Zr$_{7.5}$ 2018;7.
[17] Singh P, Marshal A, Smirnov Av, Sharma A, Balasubramanian G, Pradeep KG, et al. Tuning phase stability and short-range order through Al doping in (CoCrFeMn)100-x A lx high-entropy alloys. Physical Review Materials 2019;3:075002. https://doi.org/10.1103/PhysRevMaterials.3.075002.
[18] Sreeramagiri P, Roy A, Balasubramanian G. Effect of cooling rate on the phase formation of AlCoCrFeNi high-entropy alloy. J Phase Equilibria Diffus 2021;42:772–80. https://doi.org/10.1007/s11669-021-00918-5.
[19] Roy A, Balasubramanian G. Predictive descriptors in machine learning and data-enabled explorations of high-entropy alloys. Comput Mater Sci 2021;193:110381. https://doi.org/10.1016/j.commatsci.2021.110381.
[20] Sharma A, Balasubramanian G. Dislocation dynamics in Al0.1CoCrFeNi high-entropy alloy under tensile loading. Intermetallics 2017;91:31–4. https://doi.org/10.1016/j.intermet.2017.08.004.
[21] Johnson D, Singh R, Singh P, Sharma A, Balasubramanian G. Accelerating the computational design of multi-principle element alloys. Bull Am Phys Soc 2020;65(1).
[22] Singh R, Singh P, Sharma A, Bingol OR, Balu A, Balasubramanian G, et al. Neural-networks model for force prediction in multi-principal-element alloys. ArXiv Pre-Print Server 2021.
[23] Wu Z, Bei H, Pharr GM, George EP. Temperature dependence of the mechanical properties of equiatomic solid solution alloys with face-centered cubic crystal structures. Acta Mater 2014;81:428–41. https://doi.org/10.1016/j.actamat.2014.08.026.
[24] Roy A, Babuska T, Krick B, Balasubramanian G. Machine learned feature identification for predicting phase and Young's modulus of low-, medium- and high-entropy alloys. Scripta Mater 2020;185:152–8. https://doi.org/10.1016/j.scriptamat.2020.04.016.
[25] Průša F, Cabibbo M, Šenková A, Kučera V, Veselka Z, Školáková A, et al. High-strength ultrafine-grained CoCrFeNiNb high-entropy alloy prepared by mechanical alloying: properties and strengthening mechanism. J Alloys Compd 2020;835:155308. https://doi.org/10.1016/J.JALLCOM.2020.155308.
[26] Joress H, Decost BL, Sarker S, Braun TM, Jilani S, Smith R, et al. A high-throughput structural and electrochemical study of metallic glass formation in Ni-Ti-Al. ACS Comb Sci 2020;22:330–8. https://doi.org/10.1021/ACSCOMBSCI.9B00215/SUPPL_FILE/CO9B00215_SI_001.PDF.
[27] Chen SY, Tong Y, Liaw PK. Additive manufacturing of high-entropy alloys: a Review. Entropy 2018;20:12. https://doi.org/10.3390/e20120937.
[28] Huang C, Zhang Y, Vilar R, Shen J. Dry sliding wear behavior of laser clad TiVCrAlSi high entropy alloy coatings on Ti–6Al–4V substrate. Mater Des 2012;41:338–43. https://doi.org/10.1016/j.matdes.2012.04.049.
[29] Kunce I, Polanski M, Bystrzycki J. Structure and hydrogen storage properties of a high entropy ZrTiVCrFeNi alloy synthesized using Laser Engineered Net Shaping (LENS). Int J Hydrogen Energy 2013;38:12180–9. https://doi.org/10.1016/j.ijhydene.2013.05.071.
[30] Welk BA, Williams REA, Viswanathan GB, Gibson MA, Liaw PK, Fraser HL. Nature of the interfaces between the constituent phases in the high entropy alloy CoCrCuFeNiAl. Ultramicroscopy 2013;134:193–9. https://doi.org/10.1016/j.ultramic.2013.06.006.
[31] Yue TM, Xie H, Lin X, Yang HO, Meng GH. Solidification behaviour in laser cladding of AlCoCrCuFeNi high-entropy alloy on magnesium substrates. J Alloys Compd 2014;587:588–93. https://doi.org/10.1016/j.jallcom.2013.10.254.
[32] Kunce I, Polanski M, Bystrzycki J. Microstructure and hydrogen storage properties of a TiZrNbMoV high entropy alloy synthesized using Laser Engineered Net Shaping (LENS). Int J Hydrogen Energy 2014;39:9904–10. https://doi.org/10.1016/j.ijhydene.2014.02.067.
[33] Choudhuri D, Gwalani B, Gorsse S, Mikler CV, Ramanujan RV, Gibson MA, et al. Change in the primary solidification phase from fcc to bcc -based B2 in high entropy or complex concentrated alloys. Scripta Mater 2017;127:186–90. https://doi.org/10.1016/j.scriptamat.2016.09.023.
[34] Joseph J, Jarvis T, Wu X, Stanford N, Hodgson P, Fabijanic DM. Comparative study of the microstructures and mechanical properties of direct laser fabricated and arc-melted Al x CoCrFeNi high entropy alloys. Mater Sci Eng, A 2015;633:184–93. https://doi.org/10.1016/j.msea.2015.02.072.
[35] Borkar T, Gwalani B, Choudhuri D, Mikler CV, Yannetta CJ, Chen X, et al. A combinatorial assessment of AlxCrCuFeNi2 (0 < x < 1.5) complex concentrated alloys: microstructure, microhardness, and magnetic properties. Acta Mater 2016;116:63–76. https://doi.org/10.1016/j.actamat.2016.06.025.
[36] Choudhuri D, Alam T, Borkar T, Gwalani B, Mantri AS, Srinivasan SG, et al. Formation of a Huesler-like L21 phase in a CoCrCuFeNiAlTi high-entropy alloy. Scripta Mater 2015;100:36–9. https://doi.org/10.1016/j.scriptamat.2014.12.006.
[37] Sreeramagiri P, Bhagavatam A, Ramakrishnan A, Alrehaili H, Dinda GP. Design and development of a high-performance Ni-based superalloy WSU 150 for additive manufacturing. J Mater Sci Technol 2020;47:20–8. https://doi.org/10.1016/j.jmst.2020.01.041.
[38] Bhagavatam A, Ramakrishnan A, Adapa V, Dinda GP. Laser metal deposition of aluminum 7075 alloy. International Journal of Material Science and Research 2018;2:50–5. https://doi.org/10.18689/ijmsr-1000108.
[39] Materialgeeza. Selective laser melting system schematic n.d. https://commons.wikimedia.org/w/index.php?curid=4032088.
[40] Qin G, Xue W, Fan C, Chen R, Wang L, Su Y, et al. Effect of Co content on phase formation and mechanical properties of (AlCoCrFeNi)100-Co high-entropy alloys. Mater Sci Eng, A 2018;710:200–5. https://doi.org/10.1016/j.msea.2017.10.088.
[41] Cui W, Karnati S, Zhang X, Burns E, Liou F. Fabrication of AlCoCrFeNi high-entropy alloy coating on an AISI 304 substrate via a CoFe2Ni intermediate layer. Entropy 2019;21. https://doi.org/10.3390/e21010002.
[42] Kunce I, Polanski M, Karczewski K, Plocinski T, Kurzydlowski KJ. Microstructural characterisation of high-entropy alloy AlCoCrFeNi fabricated by laser engineered net

shaping. J Alloys Compd 2015;648:751–8. https://doi.org/10.1016/j.jallcom.2015.05.144.
[43] Chen YY, Duval T, Hung UD, Yeh JW, Shih HC. Microstructure and electrochemical properties of high entropy alloys-a comparison with type-304 stainless steel. Corrosion Sci 2005;47:2257–79. https://doi.org/10.1016/j.corsci.2004.11.008.
[44] Tong CJ, Chen MR, Chen SK, Yeh JW, Shun TT, Lin SJ, et al. Mechanical performance of the AlxCoCrCuFeNi high-entropy alloy system with multiprincipal elements. Metall Mater Trans 2005;36:1263–71. https://doi.org/10.1007/s11661-005-0218-9.
[45] Ke GY, Chen SK, Hsu T, Yeh JW. FCC and BCC equivalents in as-cast solid solutions of AlxCo yCrzCu0.5FevNiw high-entropy alloys. Ann Chimie Sci Matériaux 2006;31:669–83. https://doi.org/10.3166/acsm.31.669-684.
[46] Sistla HR, JosephW Newkirk, Frank Liou F. Effect of Al/Ni ratio, heat treatment on phase transformations and microstructure of AlxFeCoCrNi2−x (x=0.3, 1) high entropy alloys. Mater Des 2015;81:113–21. https://doi.org/10.1016/j.matdes.2015.05.027.
[47] Joseph J, Stanford N, Hodgson P, Fabijanic DM. Tension/compression asymmetry in additive manufactured face centered cubic high entropy alloy. Scripta Mater 2017;129:30–4. https://doi.org/10.1016/j.scriptamat.2016.10.023.
[48] Joseph J, Hodgson P, Jarvis T, Wu X, Stanford N, Fabijanic DM. Effect of hot isostatic pressing on the microstructure and mechanical properties of additive manufactured AlxCoCrFeNi high entropy alloys. Mater Sci Eng, A 2018;733:59–70. https://doi.org/10.1016/j.msea.2018.07.036.
[49] Karlsson D, Marshal A, Johansson F, Schuisky M, Sahlberg M, Schneider JM, et al. Elemental segregation in an AlCoCrFeNi high-entropy alloy – a comparison between selective laser melting and induction melting. J Alloys Compd 2019;784:195–203. https://doi.org/10.1016/j.jallcom.2018.12.267.
[50] Fujieda T, Shiratori H, Kuwabara K, Kato T, Yamanaka K, Koizumi Y, et al. First demonstration of promising selective electron beam melting method for utilizing high-entropy alloys as engineering materials. Mater Lett 2015;159:12–5. https://doi.org/10.1016/j.matlet.2015.06.046.
[51] Guo C, Zhou Y, Li X, Hu X, Xu Z, Dong E, et al. A comparing study of defect generation in IN738LC superalloy fabricated by laser powder bed fusion: continuous-wave mode versus pulsed-wave mode. J Mater Sci Technol 2021;90:45–57. https://doi.org/10.1016/J.JMST.2021.03.006.
[52] Sreeramagiri P, Balasubramanian G. A process parameter predictive framework for laser cladding of multi-principal element alloys. Additive Manufacturing Letters 2022;3:100045. https://doi.org/10.1016/J.ADDLET.2022.100045.
[53] Jin R, Chen W, Sudjianto A. An efficient algorithm for constructing optimal design of computer experiments. J Stat Plann Inference 2005;134:268–87.
[54] Toby BH, Von Dreele RB. GSAS-II: the genesis of a modern open-source all purpose crystallography software package. J Appl Crystallogr 2013;46:544–9. https://doi.org/10.1107/S0021889813003531.
[55] Andersson JO, Helander T, Höglund L, Shi P, Sundman B. Thermo-Calc & DICTRA, computational tools for materials science. Calphad 2002;26:273–312. https://doi.org/10.1016/S0364-5916(02)00037-8.
[56] Ramakrishnan A, Dinda GP. Direct laser metal deposition of Inconel 738. Mater Sci Eng, A 2019:1–13. https://doi.org/10.1016/j.msea.2018.10.020. 740–741.
[57] Chou HP, Chang YS, Chen SK, Yeh JW. Microstructure, thermophysical and electrical properties in AlxCoCrFeNi ($0 \leq x \leq 2$) high-entropy alloys. Mater Sci Eng B: Solid-State Materials for Advanced Technology 2009;163:184–9. https://doi.org/10.1016/j.mseb.2009.05.024.
[58] Shiue RK, Chang CT, Young MC, Tsay LW. The effect of residual thermal stresses on the fatigue crack growth of laser-surface-annealed AISI 304 stainless steel: Part I: computer simulation. Mater Sci Eng, A 2004;364:101–8. https://doi.org/10.1016/J.MSEA.2003.07.003.
[59] Park HS, Nguyen DS. Study on flaking behavior in selective laser melting process. Procedia CIRP 2017;63:569–72. https://doi.org/10.1016/J.PROCIR.2017.03.146.
[60] Naorem R, Gupta A, Mantri S, Sethi G, ManiKrishna KV, Pala R, et al. A critical analysis of the X-ray diffraction intensities in concentrated multicomponent alloys. Int J Mater Res 2019;110:393–405. https://doi.org/10.3139/146.111762.
[61] Sreeramagiri P, Balasubramanian G. Directed energy deposition of multi-principal element alloys. Frontiers in Materials 2022:103. 0. https://doi.org/10.3389/FMATS.2022.825276.